2000-04

Multiframe Temporal Estimation of Cardiac Nonrigid Motion

McEachen, John C. II; Nehorai, Arye; Duncan, James S.

IEEE

McEachen, John C., Arye Nehorai, and James S. Duncan. "Multiframe temporal estimation of cardiac nonrigid motion." IEEE Transactions on Image Processing 9.4 (2000): 651-665.

http://hdl.handle.net/10945/69336

Multiframe Temporal Estimation of Cardiac Nonrigid Motion

John C. McEachen, II, *Member, IEEE,* Arye Nehorai, *Fellow, IEEE,* and James S. Duncan, *Senior Member, IEEE*

***Abstract*—A robust, flexible system for tracking the point to point nonrigid motion of the left ventricular (LV) endocardial wall in image sequences has been developed. This system is unique in its ability to model motion trajectories across multiple frames. The foundation of this system is an adaptive transversal filter based on the recursive least-squares algorithm. This filter facilitates the integration of models for periodicity and proximal smoothness as appropriate using a contour-based description of the object's boundaries. A set of correspondences between contours and an associated set of correspondence quality measures comprise the input to the system. Frame-to-frame relationships from two different frames of reference are derived and analyzed using synthetic and actual images. Two multiframe temporal models, both based on a sum of sinusoids, are derived. Illustrative examples of the system's output are presented for quantitative analysis. Validation of the system is performed by comparing computed trajectory estimates with the trajectories of physical markers implanted in the LV wall. Sample case studies of marker trajectory comparisons are presented. Ensemble statistics from comparisons with 15 marker trajectories are acquired and analyzed. A multiframe temporal model without spatial periodicity constraints was determined to provide excellent performance with the least computational cost. A multiframe spatiotemporal model provided the best performance based on statistical standard deviation, although at significant computational expense.**

***Index Terms*—Harmonic estimation, heart motion, nonrigid motion, recursive least squares (RLS) filtering, spatiotemporal analysis.**

I. Introduction

THIS PAPER describes a new multiframe technique for tracking and quantifying the motion of a contour representing the left ventricular (LV) endocardial boundary from a sequence of two-dimensional (2-D) diagnostic medical images. The approach emerged from research [1] into the more general problem of understanding the nonrigid motion that might be associated with deformable objects' bounding contours and surfaces in images. This paper is considered a more thorough extension of initial results presented in [2]. Although LV motion is strongly three-dimensional (3-D) in reality, we intentionally constrain our efforts in this paper to two spatial dimensions to facilitate the development of multiframe temporal models of LV motion. The effectiveness of this approach becomes apparent when comparison is made between the estimated motion trajectories and the actual motion of markers implanted in the heart wall. To date, very little research has focused on the development of multiframe temporal models for the heart despite the desire to quantify wall motion over the complete cardiac cycle and the availability of *a priori* knowledge of general wall motion characteristics, especially its approximately periodic nature.

Periodic nonrigid motion can be observed throughout our daily lives in both people-made and biological forms. Some typical mechanical examples might be the deformation of a loaded automobile tire as it rolls down a highway or the surface movement of a bouncing ball. Some biological examples include the expansion and contraction of the lungs during breathing and, of course, the beating of the heart. The periodic parameter of all of these examples is obviously dependent on some environmental influences, however, in most cases when the event has reached a steady state, a cyclostationary condition can be reasonably assumed.

This is particularly true in the case of gated cardiac image acquisitions, where the acquisition process is triggered by the electrocardiographic signal (ECG). Many acquisition cycles are averaged together to produce one final image sequence. Hence, although there may be slight variations in the actual periodic parameter of the heart, the post-acquisition data does not contain this information.

A. Motivation

Measurement of physical parameters that aid in the analysis of cardiac LV function are important in assessing regional myocardial injury. Furthermore, locating regions of abnormal motion can only be done well by observing and characterizing pointwise LV wall motion. To do this, one must first obtain local point correspondences between two given frames from an image sequence of the cardiac cycle. We have previously worked on this problem using local LV shape to estimate landmarks useful for tracking [3]. However, these frame correspondences must be concatenated into a single point-tracked trajectory. The goal of this paper is to improve the performance of this technique by more coherently and elegantly taking advantage of known periodic constraints associated with heart movement.

Manuscript received November 24, 1998; revised March 23, 1999. This work was supported by the National Heart, Lung, and Blood Institute under NIH Grant R01HL44803. A. Nehorai was supported by the Air Force of Scientific Research under Grants F49620-99-1-0481 and F49620-99-1-0067, the National Science Foundation under Grant MIP-9615590, and the Office of Naval Research under Grant N00014-98-1-0542. The associate editor coordinating the review of this manuscript and approving it for publication was Dr. Michael R. Frater.

J. C. McEachen, II is with the Department of Electrical and Computer Engineering, Naval Postgraduate School, Monterey, CA 93943 USA (e-mail: mceachen@nps.navy.mil).

A. Nehorai is with the Department of Electrical Engineering and Computer Science, University of Illinois, Chicago IL 60607 USA.

J. S. Duncan is with the Departments of Diagnostic Radiology and Electrical Engineering, Yale University, New Haven, CT 06520 USA.

Publisher Item Identifier S 1057-7149(00)01501-3.

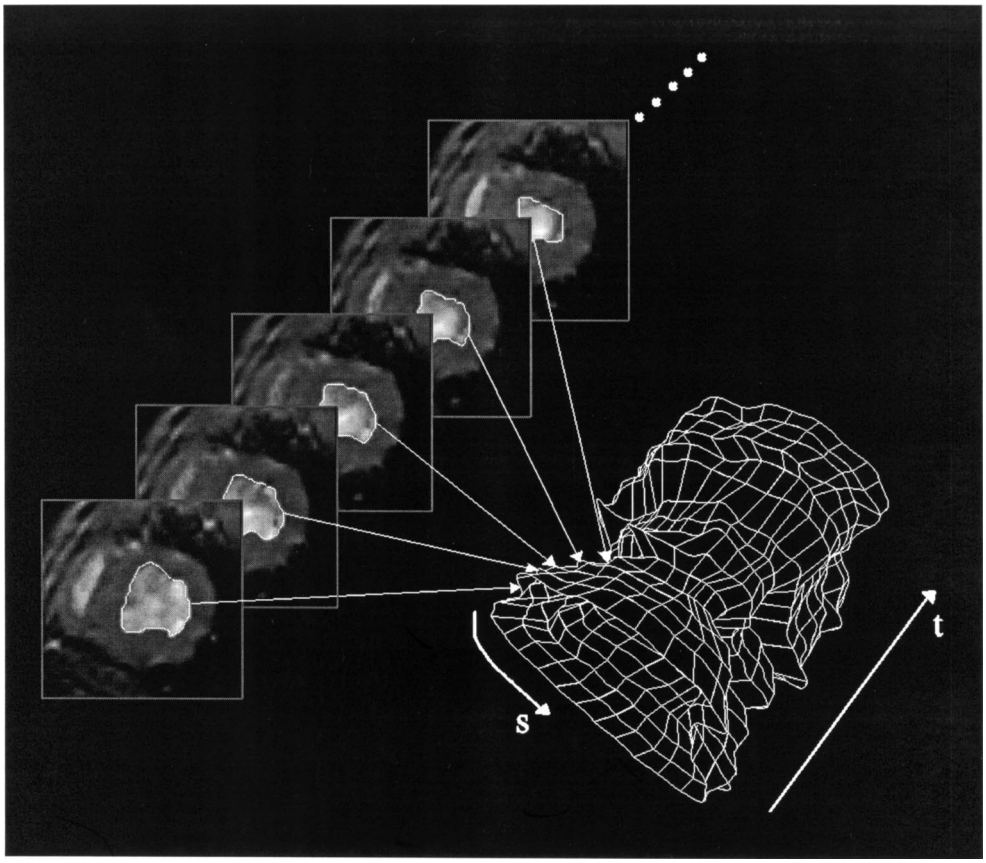

Fig. 1. Depiction of how contours are taken from their respective images and stacked in a sequence, creating a 2-D manifold in time (t) and contour space (s).

B. Related Efforts in Image Sequence Analysis

The efforts conveyed in this paper were motivated largely because of the obvious relationship of object motion to the study of natural (e.g., anatomical and/or biological) objects. This continues to be an area ripe for more attention [4], [5].

Snakes, or active contour models, have been the primary focus of many recent efforts (e.g., [6]–[11]). This method uses a physically based description of the contours to constrain the solution of movement to future frames. The physical model requires detailed prior knowledge of stiffness and mass characteristics which are often not available. Generalizations are often made to counter this problem, but this severely compromises the premise of the method in the first place. Finally, all of these methods are frame-to-frame iterations and do not take advantage of any temporal trends, particularly periodicity.

Additional efforts in 2-D tracking related to the frame-to-frame approach have been proposed [12]–[14]. The first two approaches differ in the term used for regularization of the flow vectors. Additionally, [12] uses an interpolation scheme to quantify shape between subsampled shape features. The work in [13] also optimizes a cost functional over the space of the contour, however the resulting minimization is highly nonlinear and significantly more complex due to the requirement for mapping shape-based contour correspondences back into Euclidean space values to compute the smoothing term of the functional.

The technique of harmonic analysis and enhancement used in this article is well established. While not specifically related to motion tracking, the work of [15] uses periodicity with a Fourier series to find cardiac boundaries from ultrasound sequences. Periodic models are also applied in the estimation of circular optical flow in [16].

The major thrust of research in harmonic analysis has focused on one-dimensional (1-D) signals where the fundamental frequency is unknown (e.g., [17], [18]). In contrast, the research of this article deals with a known fundamental frequency. The main contribution of this work, use of multidimensional comb filtering to constrain the system solution, is a relatively new perspective.

C. Related Efforts in Medical Imaging

The tracking of specific points on the deforming LV contour through a multiframe temporal sequence is an issue that has often been avoided by researchers within the medical imaging community. For example, many LV motion quantification approaches simply use information present in, or derived from, the end-diastolic (ED) and end-systolic (ES) image frames. The LV actually goes through a temporal wave of contraction, with different types of deformation and movement occurring at each location on the heart wall. Each point effectively follows its own unique (but locally coherent) trajectory within a 3-D Euclidean space over the time. This has been shown to be very important in studying coronary artery disease [19]. Despite this need, a fully automated, reproducible and robust approach to tracking and quantifying visually-apparent point-wise trajectories of movement on the heart wall from complete image sequences has not been previously developed.

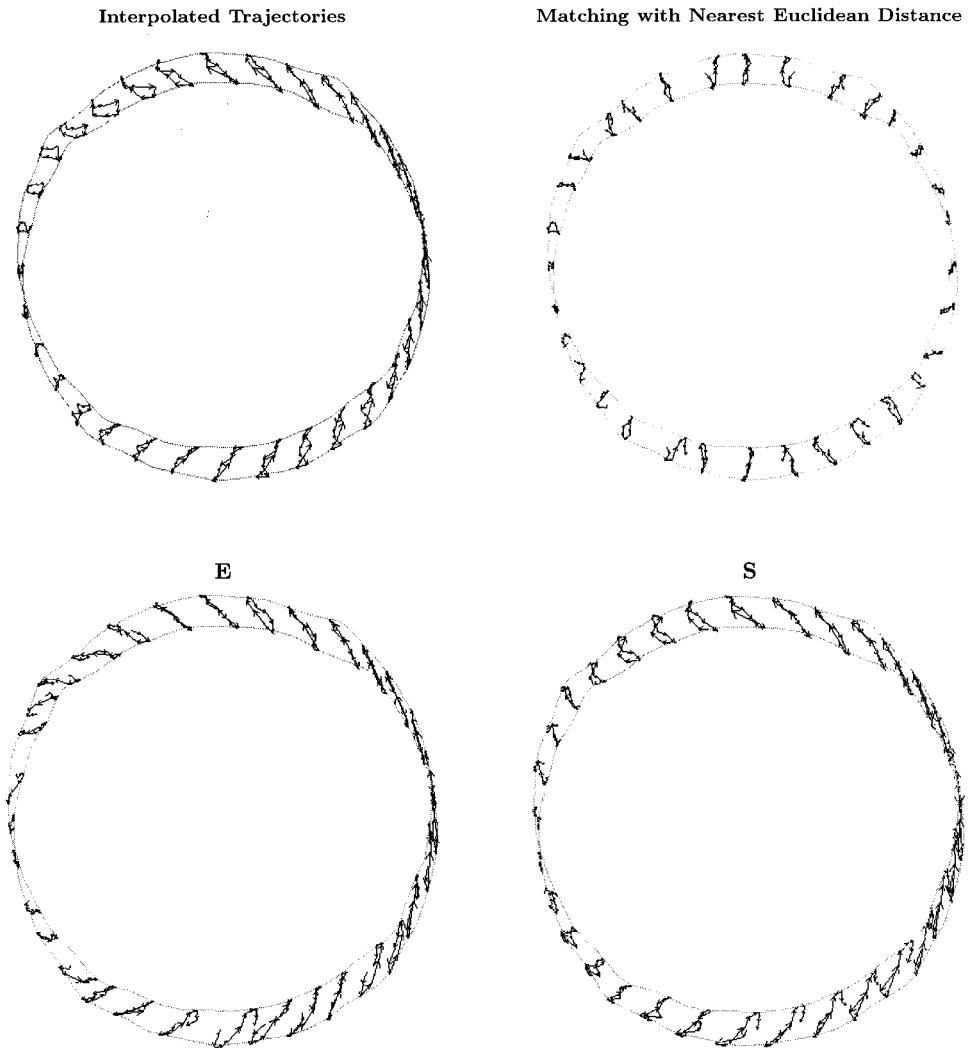

Fig. 2. Comparison of exterior phantom trajectory estimates for various frame-to-frame tracking methods. Upper left: interpolated trajectories from the landmark. Upper right: estimated trajectories using nearest Euclidean distance mapping. Lower left: estimated trajectories using the Euclidean-space method. Bottom: trajectory estimates using the contour-space method.

An approach that is noninvasive and advantageously utilizes the new imaging technology of magnetic resonance (MR) to create markers or tags is termed "MR tagging" or "MR spin-tagging" [20], [21]. This method has several drawbacks, including the fact that the tags do not typically last over the entire cardiac cycle and that the more tags there are, the poorer the background image signal to noise (making it harder to see the walls of the LV). Another key point is the denser the number of tags in each image, the more difficult the correspondence problem of matching tags between image frames in the temporal sequence, although an approach using deformable models has been proposed to address these issues [22]. The potential yield obtained by integrating these methods with geometric models, such as the one of this paper, appears significant.

Phase contrast approaches to MRI motion analysis have shown promising gains over previous MR signal encoding techniques such as spin tagging [23]. Van Dijk and others [24]–[27] have suggested use of the MR phase to record cardiac wall velocity measurements using a spin echo gated MR imaging sequence. The phase-contrast method in itself is does not appear suitable for tracking point-wise trajectories along the LV wall due to the noise associated with nonhomogeneous material along boundaries. It does, however, provide a considerable amount of general information regarding global LV motion. An attempt at incorporating phase contrast velocity information with the methods of this paper is discussed further in [28].

The study in [29] describes important research that attempts to track point trajectories over time using a sequence of images. These efforts were carefully validated using dog hearts, and are cited as a prominent supporting argument for the idea of tracking shape landmarks through time.

Several other approaches for tracking the nonrigid motion of cardiac surfaces have been offered in recent years. Most notably the work in [14], [30]–[32]. However, none of these methods addresses the requirement for a multiframe temporal model. The work in [14], specifically develops a 3-D shape-based tracking method that is analogous to the 2-D shape matching method of Section II. The potential use of this 3-D shape-matching method within the temporal framework of this article is explored further as a system extension in [33].

Some initial analysis examining the temporal aspects of cardiac motion has been done in [34] and [35]. While presenting

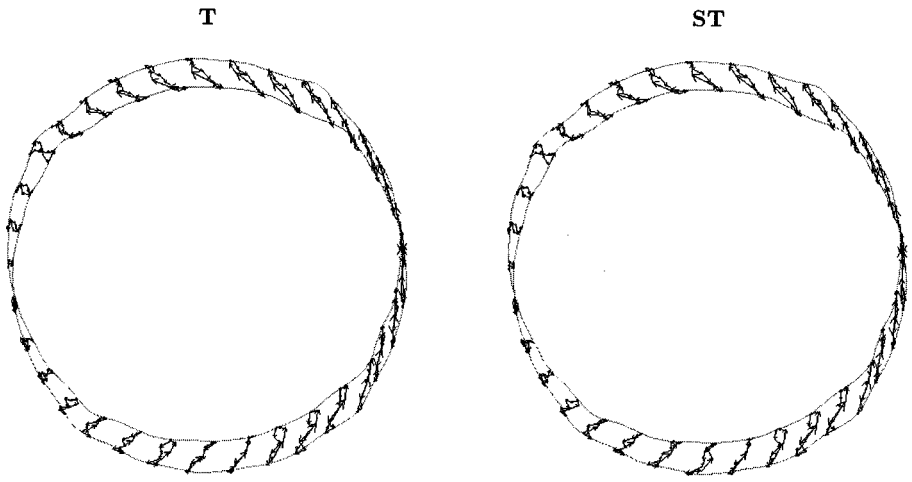

Fig. 3. Comparison of exterior phantom trajectory estimates from different configurations of RLS filter. Left: trajectory estimates using the temporal model. Right: Trajectory estimates using the spatiotemporal model.

novel approaches to modeling the temporal aspects of cardiac motion, neither of these efforts takes advantage of the *a priori* knowledge of periodicity in developing a global temporal constraint.

D. Assumptions Used in this Work

This approach to tracking and quantifying nonrigid motion, is based upon several important assumptions. First, it is assumed that the boundary of the endocardial wall must be extracted to provide an estimate of its location in each image frame. Second, it is assumed that a set of reliable tokens—segments with defined geometric properties—can be derived from the extracted boundaries. Third, the motion is such that the tokens change only a small amount from frame to frame. Finally, the wall motion is assumed to be approximately periodic. Given these assumptions an algorithm has been developed for computing nonrigid object motion from a sequence of images.

The object boundary is modeled as a closed deformable contour using a parametric model as discussed in [36]. A sequence of contours output from this method provides input for our multiframe nonrigid motion tracking system. The presentation of this system begins with a review of previous methods [1], [3] for frame-to-frame motion tracking that led to the development of the present temporal models. Two temporal models are then derived based on assumptions of periodicity. An adaptive filtering framework is derived based on these models and our frame-to-frame proximal relationship. Experiments on synthetic and actual medical images are performed and quantitative comparisons with trajectories of actual implanted markers are evaluated for single cases as well as a small ensemble of sequences.

II. Frame-to-Frame Estimation

In this approach, initial correspondences between points on a given contour $\mathcal{C}_i$ and points on a successive displaced contour $\mathcal{C}_{i+1}$ in the sequence are found by matching shape properties of contour segments surrounding each of the points as described in [37]. Two sets of corresponded points result: An originally ordered, monotonically increasing set, indexed by $m_i = m = [0, N]$ on the contour found at t_i, and a corresponded set, indexed by $m^*_{i+1} \in [0, N]$ that are established on the contour at t_{i+1}. This mapping can be viewed as an the initial estimate of a final mapping.

One additional outcome of this process is match confidence measures. The need for confidence measures is brought about by notions of 1) how matches in any one region are treated in the sense of their relative strength when compared with matches created in other local regions and 2) how decisions are handled in regions where there are many plausible matches. Thus, the strength and uniqueness of a match are used to help drive the solution of the overall flow field. Guided by the work in [38], two confidence measures modeling these characteristics are defined, both based upon the profile of the bending energy within each match search region. Details of the derivations of these values are presented in.

The objective at this juncture is to find a vector flow field that corresponds points on two contours found from two consecutive temporal frames in an image sequence by seeking a compromise between adhering to the points where the segments of the contours best match and adhering to the model where adjacent points on the contour move smoothly. Two possible approaches to solving this problem have been proposed, each having potential advantages and disadvantages. These two approaches are described in greater detail in [3].

The first approach, referred to herein as the Euclidean space model, views the initial shape matched correspondences as a collection of vectors in the Euclidean space of the image. Specifically, the normal and tangential components of the vector associated with the shape match from point m_i on the initial contour to point m^*_{i+1} on the displaced contour are stacked into a vector. Combining this with a first order difference operator and a diagonal match confidence matrix, the solution of the resulting optimization problem yields a best compromise between shape match adherence and smooth proximal. Once the smooth flow field has been computed, the resulting vectors may or may not extend from the first contour to the second. This occurs because the above functional contains no explicit constraint on the feasible solution space. Currently, this is overcome by simply mapping each vector to its closest point on the second contour. Un-

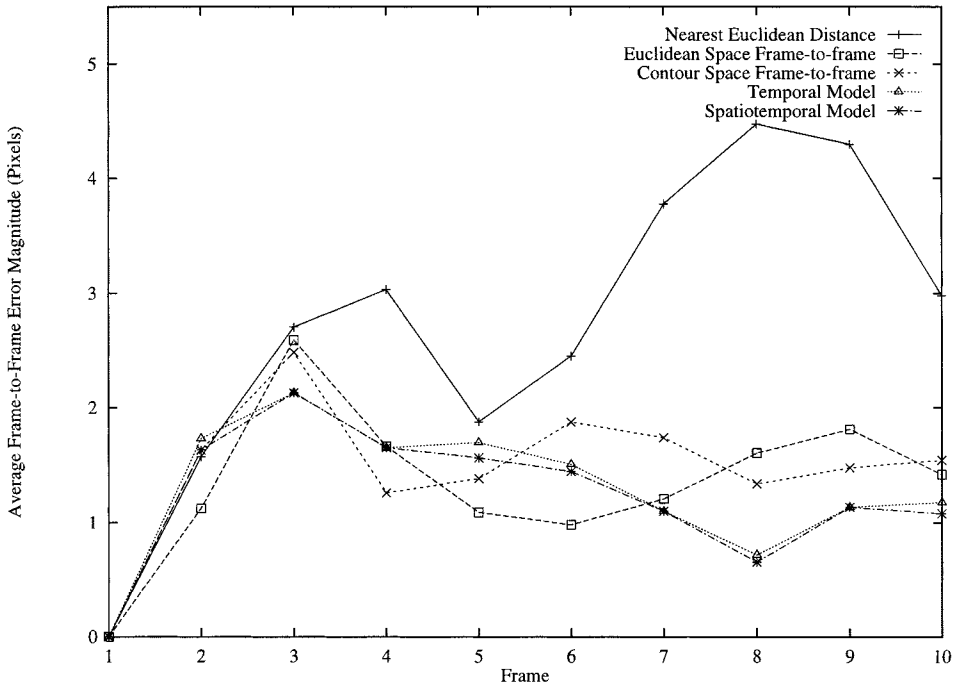

(a)

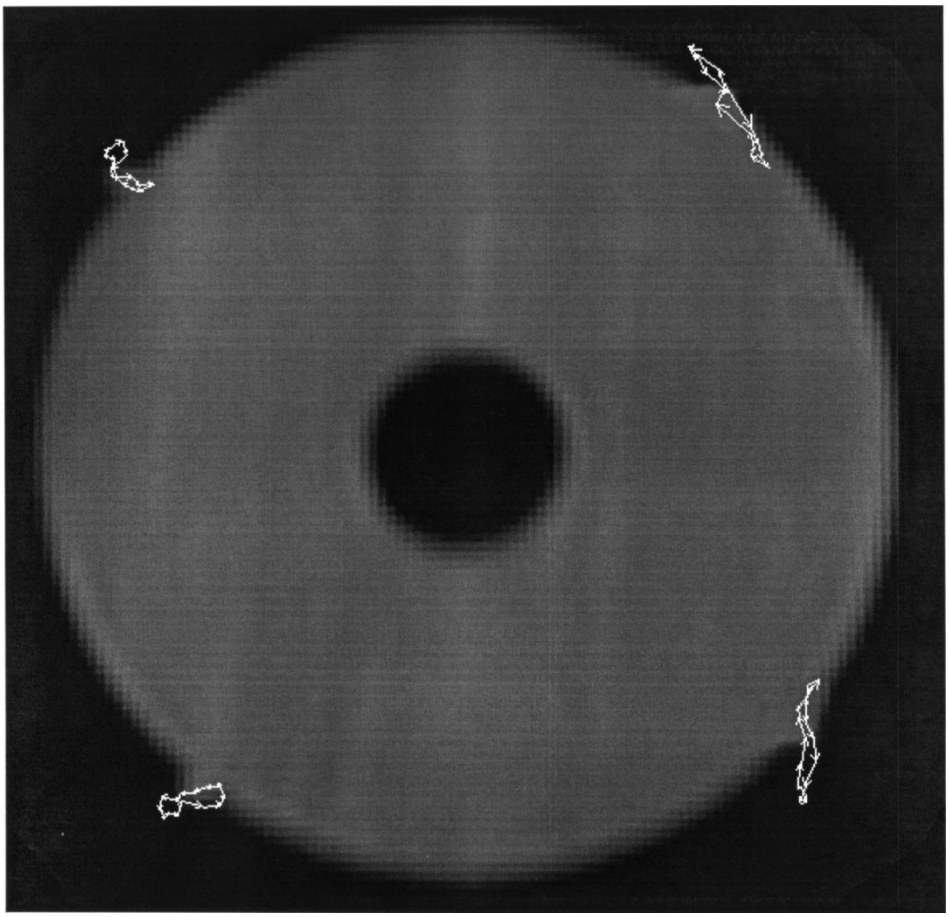

(b)

Fig. 4. (a) Average error magnitude over all trajectory estimates at a given frame for the phantom experiment illustrated in Figs. 2 and 3. (b) Sample image of the object in rigid motion used for initial verification of the tracking system. The bumps at 45, 135, 225, and 315° are considered landmarks for tracking. The overlaid white vectors are the trajectories of the landmarks as they travel through the motion test sequence.

fortunately, this occasionally results in awkward or physically implausible mappings. This characteristic and the associated accumulated noise limit this method's utility for further development with temporal models.

The second approach, referred to as the contour space model, constrains the solution space of the optimization problem to the displaced contour. The mapping from a given point, m_i, on the initial contour to a point, m^*_{i+1}, on the displaced contour is characterized by an increasing, monotonic function, $\phi_i(m_i) = m^*_{i+1}$. Discrete values of $\phi_i(m_i)$ are stacked to form a mapping vector, $\mathbf{m}^{shape}$. Again, as described in [3], a diagonal confidence matrix is defined, $\mathbf{C}$. In this situation, $\phi_i(m_i)$ is encouraged to adhere to a one-to-one relationship, hence a second order difference matrix, $\mathbf{DD}$, is used where $\mathbf{D}$ is a first order difference operator. The cost function for the best estimate, $\mathbf{m}^*$, of the mapping vector is then

$$\begin{aligned}\mathbf{m}^* &= \arg\min_{\mathbf{m}}[F] \\ &= \arg\min_{\mathbf{m}}\left[(\mathbf{m}-\mathbf{m}^{shape})^T\mathbf{C}(\mathbf{m}-\mathbf{m}^{shape})\right. \\ &\qquad \left.+\mathbf{m}^T\mathbf{D}^T\mathbf{D}^T\mathbf{DDm}\right]. \end{aligned} \tag{1}$$

The global minimum of this convex function is

$$\mathbf{m}^* = (\mathbf{C}+\mathbf{D}^T\mathbf{D}^T\mathbf{DD})^{-1}\mathbf{Cm}^{shape}. \tag{2}$$

The vector $\mathbf{m}^*$ can be viewed as the nearest local minimum on this optimization surface which qualitatively represents a vector flow field that contains a compromise between 1) the best local matches for all points on the first contour to the second contour, with each match being weighted according to uniqueness of the shape in the match region and 2) requiring each of these vectors to have a magnitude and direction that smoothly agrees with its spatially neighboring vectors. Additionally, posing the optimization problem in the contour space implicitly constrains the displacement vectors to the contours themselves. It also forces the solution to be a linear filter.

III. Multiframe Estimation

The representation of endocardial motion of the previous section is periodic in both contour space ($m_i \in [0, N]$) and time ($i \in [0, T]$). This is a unique aspect of the problem of tracking LV wall motion in 2-D which has not been previously exploited. In both models presented in this section, all the frame-to-frame continuous mapping functions of an image sequence are consolidated into one 2-D function, $\phi(s, t)$, representing the entire manifold (Fig. 1). With a spatial constraint (local smoothness) incorporated into the frame-to-frame relationship of the previous section, we first concentrate on modeling the temporal dimension alone using a sum of sinusoids. The next section examines an extended spatiotemporal version of this model coupling periodic trends over both contour space and time. The superscripts (T) and (ST) are used in these two sections exclusively to delineate between variables ($\eta^{(T)}$, $\Xi^{(T)}$) modeled after the temporal dimension alone and variables ($\eta^{(ST)}$, $\Xi^{(ST)}$) employing spatiotemporal modeling.

TABLE I
Quantitative Comparisons of Trajectory Estimates Made from Nearest Euclidean Distance Correspondence (N), Euclidean Space Regularization (E), Contour Space Regularization (S), Recursive Filtering Using the Temporal Model (T), and Recursive Filtering Using the Spatiotemporal Model (ST) with Trajectories Interpolated from the Four Landmarks as Shown in Figs. 2 and 3

Method	Mean Err.	Std. Dev. of Mean Err.	Avg. Temp. Std. Dev.	Avg Mean Disp. Err.	Std. Dev. Disp. Err.
N	2.72	1.36	1.89	0.603	0.626
E	1.35	0.648	1.45	0.0531	0.472
S	1.47	0.861	1.22	0.313	0.654
T	1.28	1.12	1.06	0.0153	0.648
ST	**1.24**	**1.13**	**1.03**	**0.0425**	**0.564**

A. Modeling Temporal Periodicity

The continuous periodic mapping function, $\phi(s, t)$, referenced above, can be viewed as a sum of sine waves whose frequencies are integral multiples of the lowest (or fundamental) frequency. Such a function is said to be harmonic. The trajectory of a single discrete point, s_o, on this spatiotemporal manifold can be approximately modeled as follows:

$$\begin{aligned}\phi(s_o, i) &= m_i \\ &= \sum_{r=1}^{R} A_r \sin(r\omega_o i + \gamma\psi_r)\end{aligned} \tag{3}$$

where $\omega_o = (2\pi/T)$ is the fundamental frequency of the contour deformation over time. The index r represents harmonics of ω_o. A_r and ψ_r are the amplitude and phase of the (r)th harmonic component of m_i. R is assigned to represent the highest significant harmonic of ω_o and i represents a discrete time frame within the range of t.

Through standard trigonometric manipulation, (3) can be expressed as

$$m_i = \sum_{r=1}^{R} g_r \cos(r\omega_o i) + h_r \sin(r\omega_o i) \tag{4}$$

where $g_r = A_r \sin(\psi_r)$ and $h_r = A_r \cos(\psi_r)$.

If we assign $\xi_i = [\cos(\omega_o i)\cdots\cos(r\omega_o i)\cdots\cos(R\omega_o i), \sin(\omega_o i)\cdots\sin(r\omega_o i)\cdots\sin(R\omega_o i)]$ and $\eta_m = [g_1\cdots g_r\cdots g_R, h_1\cdots h_r\cdots h_R]^T$ (4) can be expressed as a vector product

$$m_i = \xi_i\eta_m. \tag{5}$$

Note that (5) represents a single trajectory $\forall i \in [0, T]$ (where T is the number of frames in the image sequence). We wish to develop an expression for each of the N trajectories associated with our frame-to-frame mapping vector, $\mathbf{m}_i$, that will allow us to define a system equation in subsequent sections. Values of (5) $\forall m_i \in \mathbf{m}_i$ and a given frame, i, can be determined using the following vector product:

$$\mathbf{m}_i = \Xi_i^{(T)}\eta^{(T)} \tag{6}$$

where $\eta^{(T)} = [\eta_1^T \cdots \eta_m^T \cdots \eta_N^T]^T$ and $\Xi_i^{(T)}$ is

$$\begin{pmatrix} [& \xi_i &] & 0 & \cdots & 0 & \cdots & & 0 & \\ 0 & \cdots & 0 & [& \xi_i &] & 0 & & \vdots & \\ \vdots & \ddots & & 0 & \cdots & 0 & \ddots & 0 & \cdots & 0 \\ 0 & & & \cdots & & & 0 & [& \xi_i &] \end{pmatrix}.$$

$\Xi_i^{(T)}$ is of size $N \times 2RN$ and represents the cosine and sine terms for a given i. $\Xi_i^{(T)}$ can be viewed as a sinusoidal basis transformation matrix. $\eta^{(T)}$ is of size $2RN \times 1$ and represents phases and amplitudes of harmonic components. $\eta^{(T)}$ can be viewed as a sinusoidal parameterization of the entire manifold (i.e., all of the harmonic trajectory information is contained within $\eta^{(T)}$).

B. Modeling Spatiotemporal Periodicity

As stated at the beginning of this section, the representation of endocardial motion employed in this system is periodic in both contour space ($m_i \in [0, N]$) and time ($i \in [0, T]$). Section III-A presented a model focused solely on the temporal prior. In this section, a model is constructed that is based on the periodic nature of both time and contour space.

As before, all the continuous mapping functions are consolidated into one 2-D function, $\phi(s, t)$, and expressed as a sum of sinusoids. This time, however, a term dependent on contour space, s, is included. Recall s represents arclength of a contour that is typically closed, hence s is periodic in nature. A more general form of (3) is defined as

$$\phi(s,i) = \sum_{q=1}^{Q} \sum_{r=1}^{R} A_{q,r} \sin(q\upsilon_o s + r\omega_o i + \psi_{q,r}) \tag{7}$$

where $\upsilon_o = (2\pi/N)$ is the fundamental frequency over the space of the contour and $\omega_o = (2\pi/T)$ is the fundamental frequency of the cardiac cycle over time. The index q represents harmonics of υ_o, and similarly r indexes ω_o. $A_{q,r}$ and $\psi_{q,r}$ are the amplitude and phase of the (q, r)th harmonic component of $\phi(s, t)$, respectively. Q and R represent the highest significant harmonics of υ_o and ω_o, respectively, and i represents a discrete time frame within the range of t.

Through standard trigonometric manipulation this can be expressed as

$$\begin{aligned}\phi(s,\, i) = &\sum_{q=1}^{Q} \sum_{r=1}^{R} g_{q,r} \cos(q\upsilon_o s + r\omega_o i) \\ &+ h_{q,r} \sin(q\upsilon_o s + r\omega_o i)\end{aligned} \tag{8}$$

where $g_{q,r} = A_{q,r} \sin(\psi_{q,r})$ and $h_{q,r} = A_{q,r} \cos(\psi_{q,r})$. For the purpose of developing a system equation, (8) can be converted into a vector product in the following manner for a given frame i:

$$\mathbf{m}_i = \Xi_i^{(ST)} \eta^{(ST)} \tag{9}$$

where $\mathbf{m}_i$ is the mapping function for frame i, $\eta^{(ST)} = [g_{1,1} \cdots g_{1,R},\, g_{2,1} \cdots g_{2,R} \cdots g_{Q,R},\, h_{1,1} \cdots h_{Q,R}]^T$, and $\Xi^{(ST)}$ is the dimension $N \times 2QR$. $\eta^{(ST)}$ of dimension $2QR \times 1$.

As in Section III-A, $\eta^{(ST)}$ represents a parameterization of the entire manifold suitable for use as a state vector. It is important to note that although we arrived at a definition for $\Xi^{(ST)}$ and $\eta^{(ST)}$ in a manner similar to the definition of $\Xi^{(T)}$ and $\eta^{(T)}$, $\Xi^{(ST)}$ and $\eta^{(ST)}$ of this section are a significantly different representation of $\phi(s, t)$ than those derived in the previous section.

C. Adaptive Estimation

The design of a Wiener filter [39], which is optimum in the mean-square sense, requires *a priori* information about the statistics of the data processed. When *a priori* information is not available, the Wiener filter design is either not possible or no longer optimum. An efficient alternative approach that may be used in such situations is an adaptive filter.

An adaptive filter is a self-designing device that relies on a recursive algorithm for its operation. The use of a recursive algorithm makes it possible for the filter to perform in environments where complete knowledge of the relevant signal characteristics is not available. In a stationary environment, the recursive algorithm actually converges to the optimum Wiener solution in a statistical sense after successive iterations [40].

The classic method of least squares approach differs from Wiener filtering in that it is deterministic in its formulation from the start. The method of least squares minimizes an index of performance consisting of the sum of weighted error squares, where the error is defined as the difference between some observed response and the actual filter output. The recursive least squares (RLS) algorithm uses a transversal filter similar to a Wiener filter as the structural basis of the adaptive filter.

The above reasoning supports the use of an RLS driven adaptive filter for estimating pointwise cardiac motion trajectories. To date, no statistical information is available or can be reasonably approximated that accurately represents pointwise cardiac motion. Consequently, our approach to cardiac motion analysis is purely deterministic in nature. Additionally, the linear models developed in Sections II, III-A, and III-B facilitate the use of a transversal filter.

The shape-based correspondence vectors, $\mathbf{m}_i^{shape} \forall i \in [1, T]$, are viewed as the observed response in the RLS scheme. Either $\eta^{(T)}$ or $\eta^{(ST)}$ may be substituted for η in the following section depending on the choice of temporal model from Section III-A. Equation (2) established a relationship that will define the observation equation. If we assign $\mathbf{H} = (\mathbf{C} + \mathbf{D}^T\mathbf{D}^T\mathbf{D}\mathbf{D})^{-1}\mathbf{C}$ (recall that $\mathbf{C}$ represents the correspondence confidence matrix and $\mathbf{D}$ is a first order difference operator), and note that $\mathbf{H}$ is positive definite, (2) and (6) can be combined as $\mathbf{m}_i^{shape} = \mathbf{H}_i^{-1}\Xi_i\eta + \upsilon_i$ where υ_i represents observation error at frame i due to the truncation of harmonics, proximal smoothing and the accompanying ill-determined relationship ($\dim \mathbf{m_i} \neq \dim \eta$). Recall that Ξ_i is the sinusoidal basis transformation matrix of Sections III-A and III-B, where the choice between $\Xi^{(T)}$ and $\Xi^{(ST)}$ depends on the selection of temporal model. For convenience we assign $\mathbf{G}_i = \mathbf{H}_i^{-1}\Xi_i$. This provides us with the following:

$$\mathbf{m}_i^{shape} = \mathbf{G}_i\eta + \upsilon_i. \tag{10}$$

Equation (10) is considered the observation equation because it relates the data-derived shape-based mapping to the state vector.

The following development of the RLS filter is based upon work in [41]. The difference between our observed values, $\mathbf{m}_i^{shape}$, and the estimated mappings, $\mathbf{G}_i\eta$, in (10) is the observation error, v_i, hence the index of performance we wish to minimize, Υ, is defined as follows:

$$\Upsilon = \sum_{n=1}^{N} |v_n|^2 \tag{11}$$

where N remains the $\dim \mathbf{m}$. The optimum value of $\hat{\eta}$ for which the performance index, Υ, attains its minimum value is obtained by solving the classic least squares relationship

$$\Phi_n \hat{\eta} = \Theta_n \tag{12}$$

where the correlation matrix Φ_n is of size $2RN \times 2RN$ or $2QR \times 2QR$, depending on the temporal model ($\Xi^{(T)}$ or $\Xi^{(ST)}$—R is the number of temporal harmonics, Q the number of spatial harmonics). Φ_n is defined by

$$\Phi_n = \sum_{i=1}^{n} \mathbf{G}_i^T \mathbf{G}_i. \tag{13}$$

Θ_n represents the cross-correlation of $\mathbf{m}^{shape}$ and $\mathbf{G}$ as

$$\Theta_n = \sum_{i=1}^{n} \mathbf{G}_i^T \mathbf{m}_i^{shape}. \tag{14}$$

A recursive relationship for Φ_n may be derived by first isolating the term corresponding to $i = n$ from the rest of the summation, allowing (13) to be written as

$$\Phi_n = \Phi_{n-1} + \mathbf{G}_n^T \mathbf{G}_n. \tag{15}$$

Note that the matrix $\mathbf{G}_n^T \mathbf{G}_n$ plays the role of a corrective term.

In a similar fashion, (14) can be used to derive the following recursion for updating the deterministic cross-correlation vector:

$$\Theta_n = \Theta_{n-1} + \mathbf{G}_n^T \mathbf{m}_n^{shape}. \tag{16}$$

To compute the least-square estimate of $\hat{\eta}$ for $\mathbf{G}$ in accordance with (12), the inverse of the correlation matrix, Φ_n, needs to be determined. If we let $\mathbf{P}_n = \Phi_n^{-1}$, using basic inversion techniques, $\mathbf{P}_n$ can be expressed as

$$\mathbf{P}_n = \mathbf{P}_{n-1} - \mathbf{K}_n \mathbf{G}_n \mathbf{P}_{n-1} \tag{17}$$

where $\mathbf{K}_n$ is the RLS gain matrix and is defined by

$$\mathbf{K}_n = \mathbf{P}_{n-1} \mathbf{G}_n^T (\mathbf{I}_N + \mathbf{G}_n \mathbf{P}_{n-1} \mathbf{G}_n^T)^{-1}. \tag{18}$$

The final step in our RLS formulation is to develop a recursive equation for updating the least-squares estimate of $\hat{\eta}$ at iteration n. Using (12), (16), and (17) the new estimate of the state vector is formed

$$\hat{\eta}_n = \hat{\eta}_{n-1} + \mathbf{K}_n (\mathbf{m}_n^{shape} - \mathbf{G}_n \hat{\eta}_{n-1}). \tag{19}$$

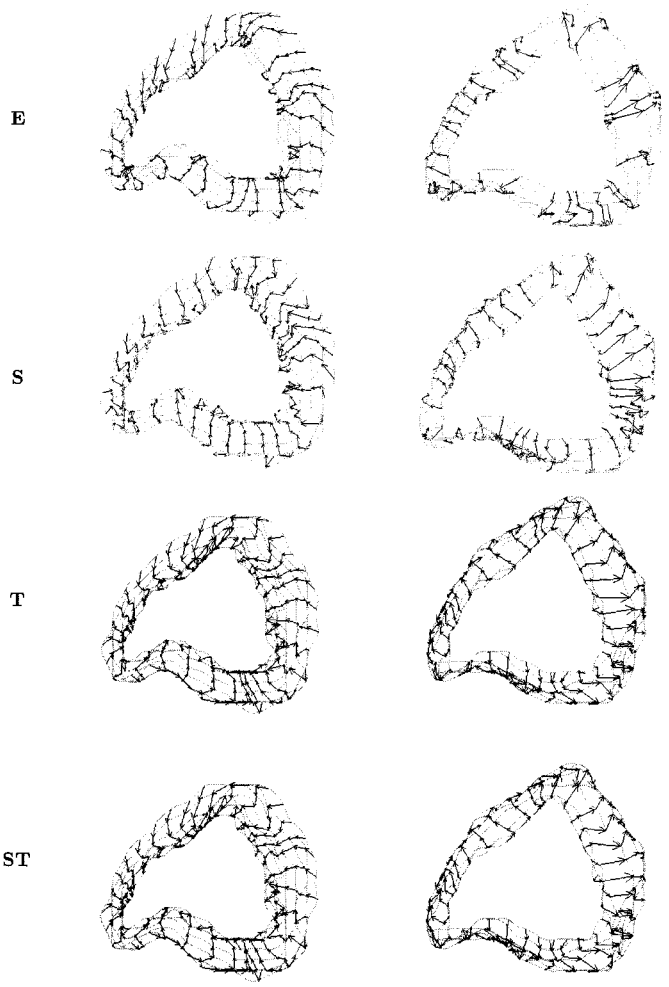

Fig. 5. Qualitative comparison of trajectory estimates from all configurations for a typical image sequence. Clarity is achieved in this case by dividing the sequence in half-frames one through ten (on left) (ED to ES), and frames 11 through 16 (on right) (ES to ED). Note the divergence of trajectories estimated with the frame-to-frame methods as compared to those from the RLS filter.

The rightmost term of (19) is referred to as the *a priori estimation error* and is defined as $\alpha_n = \mathbf{m}_n^{shape} - \mathbf{G}_n \hat{\eta}_{n-1}$. The product $\mathbf{G}_n \hat{\eta}_{n-1}$ represents an estimate of the observed response based on the old least squares estimate of the state vector, η, that was made at time $n-1$.

The single constraint on the initial conditions of the RLS algorithm is imposed by (17). $\mathbf{P}_0$ must be chosen so that the covariance matrix, Φ_0, is nonsingular. For the experiments of this article, $\mathbf{P}_0 = \Delta \mathbf{I}$, where $\Delta \approx 10\,000$. This causes values of $\mathbf{K}$ to be nearly 1, thus forming initial estimates based primarily on the observed data until the system learns further information about temporal trends. The choice for the initial value of the state vector, $\eta_0 = \mathbf{0}$, is illustrative of the initial lack of statistical knowledge associated with this problem.

The final state of $\hat{\eta}$ is retrieved after successive iterations of the adaptive filter have satisfied $|\alpha_{Tn} - \alpha_{(T-1)n}| < 0.01$ where T is the number of frames in the image sequence. The value 0.01 was chosen because it represents an average error of 0.1 pixels—enough to ensure no change occurs between cyclic iterations of discrete mapping function versions. The quantity T is incorporated to ensure the information from a complete image

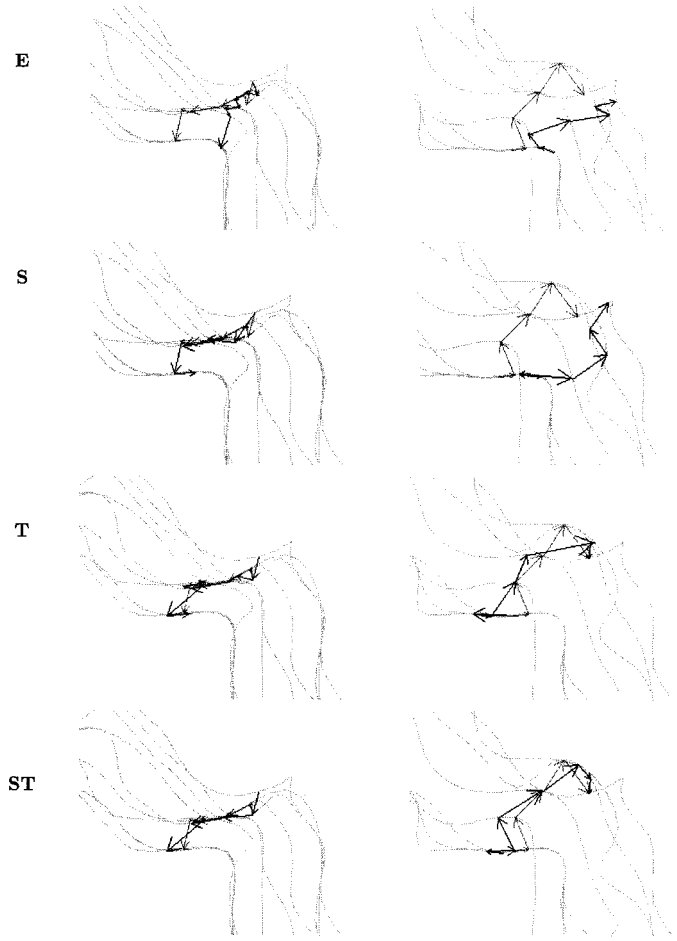

Fig. 6. Comparison of estimated trajectories for each tracking method with the marker. Each graphic is divided into two temporal sections for clarity. Estimated trajectory is in black. Marker trajectory is in grey. As before, the graphics are divided into two temporal sections, frames 1–9 on the left and frames 10–16 on the right. Note how closely RLS filtering with the spatiotemporal model (ST) estimates the true trajectory.

TABLE II
QUANTITATIVE ANALYSIS OF THE TRAJECTORIES SHOWN IN FIG. 6

Method	# Harmonics	Max Err.	@ Frame	Mean Err.	Std. Dev.	Mean/Disp.
E	NA	2.55	15	1.05	0.69	1.22
S	NA	3.00	15	0.98	0.87	1.18
T	16	1.37	11	0.61	0.50	0.70
ST	**16**	**1.32**	**5**	**0.55**	**0.40**	**0.65**

sequence cycle is considered before the filter iteration is brought to a halt. In the case of the temporal model, substantial computational reductions, on the order of N^2 multiplications, can be realized by taking advantage of the highly banded nature of the error covariance matrix, $\mathbf{P}_n$.

The solution mapping is determined by carrying out the following assignment $\forall i$: $\hat{\mathbf{m}}_i^* = \Xi_i \hat{\eta}$. This final mapping represents a shape-driven, spatially and temporally smooth, and periodically constrained solution to the posed problem.

IV. SYSTEM EXPERIMENTS

The intent of this section is to provide a thorough examination of the relevant critical parameters of system performance. First, an image sequence of simulated motion is analyzed to verify basic intentions of system design and performance. Studies of sample cardiac image sequences are then presented for qualitative evaluation. Validation comparisons are made with the motion of physical markers actually implanted in the heart wall. Finally, an ensemble of cardiac image sequences is examined to obtain a statistical sense of system performance in general.

For brevity, the following abbreviations are used in tables and figures throughout this section to denote the various filtering methods described in Sections II and III: (E)—Euclidean-space frame-to-frame tracking; (S)—Contour-space frame-to-frame tracking; (T)—RLS filtering employing the temporal model; and (ST)—RLS filtering employing the spatiotemporal model. (NA is not applicable). Rows of tables in boldface highlight the best performance parameters of the group under consideration.

A. Evaluation

The noninvasive requirement for tracking cardiac motion makes verification of estimated trajectories particularly difficult. Additionally, as we will see with the imaged phantom, even pointwise trajectories of a known global rigid motion are not entirely intuitive. A clearly visible implanted marker may be used to provide a reference landmark on the LV wall, however, this represents one trajectory of many along an entire contour which by its very nature deforms differently in different regions. Details of the marker implantation technique can be found in [29]. Unfortunately, implanting more than a few markers along the LV wall increases the amount of stress the heart is under and causes the heart to function abnormally or not at all.

Consequently, both qualitative evaluation and marker comparison should be considered in appraising the performance of the methods of this article. Qualitative assessments provide a general idea of the shape-related motion for all points over the image sequence. Marker comparisons provide a measure of locally specified motion.

The magnitude of the difference between estimated correspondence and marker location in Euclidean space is the method of error measurement used predominantly throughout this section. This error measure was chosen because knowing the correspondence location at each point in time and the temporal correspondence flow over the sequence are the primary objectives of the trajectory estimates and the most appropriate basis for further strain analysis. Additionally, the standard deviation of the error is used as a significant measure of trajectory flow error because it highlights consistency in the mean error measurement.

Quantitative assessments of marker comparisons are presented in tables throughout this section. Specific categories of data examined are as follows.

Max Error	Maximum single frame distance, in pixels, between the marker correspondence and the estimated correspondence occurring over all frames of the sequence.
@ Frame	Frame at which the maximum single frame error occurred.
Mean Error	Mean distance between the marker correspondence and estimated corre-

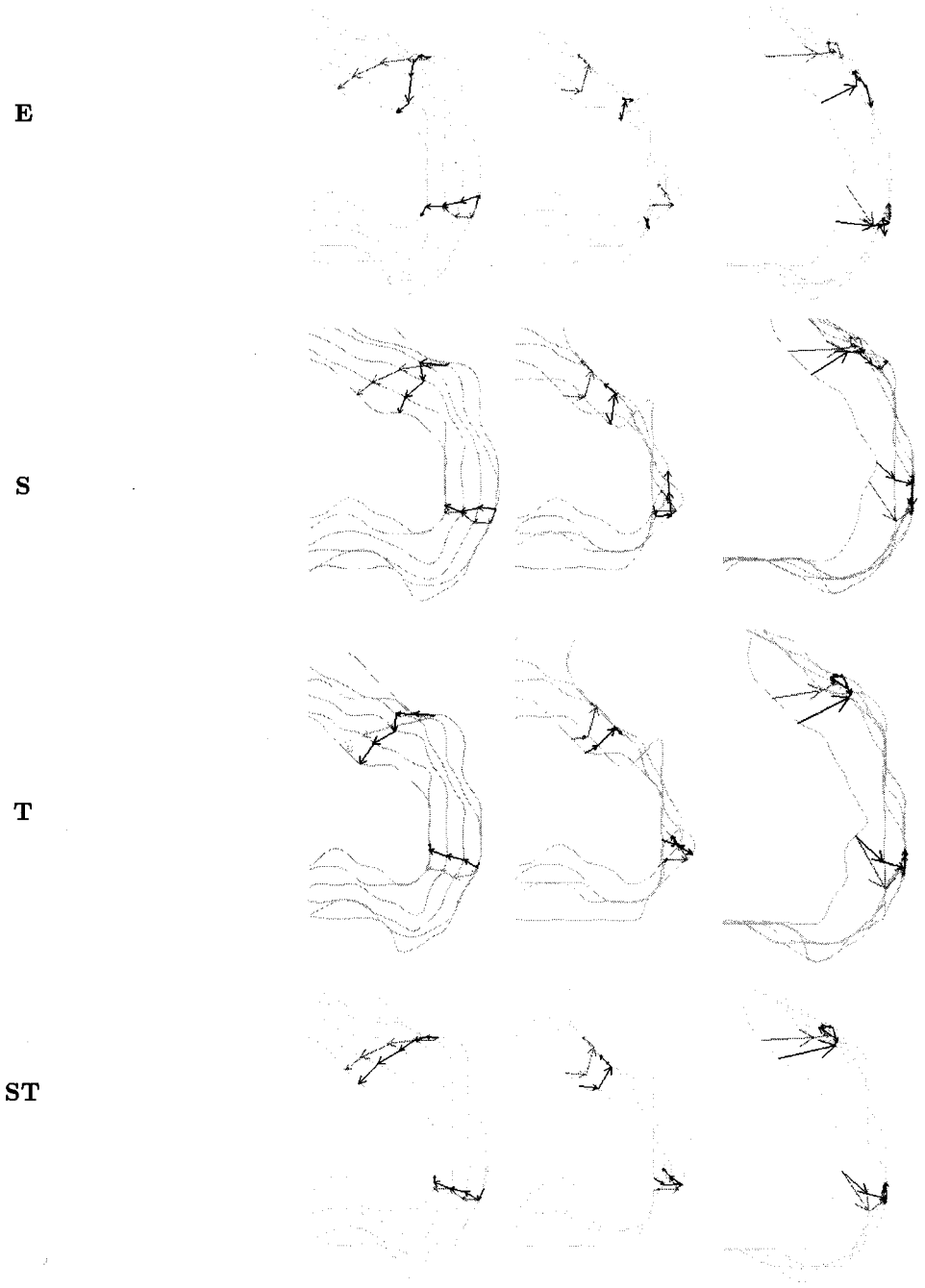

Fig. 7. Comparison of trajectory estimates with two corresponding implanted marker trajectories. The sequence is divided into three temporal sections for clarity. Top: trajectories estimated with the Euclidean space frame-to-frame approach (shown in black) compared with marker trajectories (shown in grey). Upper middle: trajectories estimated with the contour space frame-to-frame approach (shown in black) compared with marker trajectories (shown in grey). Lower middle: RLS filtered trajectories estimated with the temporal model (shown in black) compared with marker trajectories (shown in grey). Bottom: RLS filtered trajectories estimated with the spatiotemporal model (shown in black) compared with marker trajectories (shown in grey).

	spondence, in pixels, computed for all frames of the sequence.
Std. Dev.	Standard deviation of the correspondence error, in pixels, computed for all frames of the sequence.
Mean Disp. Error	Average difference in trajectory displacement, in pixels, computed for all frames of the sequence.
Mean/Disp.	Mean of the single frame correspondence error divided by marker displacement over all frames of the sequence.

B. Simulated Motion

To provide an initial testing environment, a cylindrical phantom Fig. 4(b) was imaged (512 × 512 pixels) as it underwent a periodic rigid arcing motion. The exterior of the phantom had four distinct shape landmarks for use in verifying tracking methods. Figs. 2 and 3 are provided to allow qualitative

TABLE III
QUANTITATIVE ANALYSIS OF THE TRAJECTORIES SHOWN IN FIG. 7. MARKER 1 REPRESENTS THE UPPER TRAJECTORY IN FIG. 7

Marker 1:

Method	# Harmonics	Max Err.	@ Frame	Mean Err.	Std. Dev.	Mean/Disp.
E	NA	3.97	10	2.36	1.22	3.26
S	NA	2.65	6	1.38	0.92	1.88
T	15	2.30	9	0.87	0.67	0.95
ST	**15**	**1.53**	**8**	**0.74**	**0.56**	**0.91**

Marker 2:

Method	# Harmonics	Max Err.	@ Frame	Mean Err.	Std. Dev.	Mean/Disp.
E	NA	2.16	9	0.92	0.73	1.20
S	NA	2.36	11	0.72	0.66	1.10
T	15	1.44	5	0.66	0.50	1.03
ST	**15**	**0.97**	**11**	**0.31**	**0.33**	**0.48**

evaluation of trajectory estimates around the entire cylinder. In this example, 32 trajectories are illustrated. Trajectories interpolated from the movement of the four landmarks are used as the defining standard. Trajectories estimated using nearest Euclidean distance correspondence [42] are provided as a control reference. We note how our methods using frame-to-frame regularization in Euclidean space and contour space both do a satisfactory job of capturing the rigid arcing motion of the cylinder. This is in stark contrast to the trajectories estimated with basic nearest Euclidean distance mapping. We also note, however, that both frame-to-frame filtering methods fail to return to their origin. This problem is solved using recursive filtering with temporal models as shown in Fig. 3. The trajectories in this instance appear to be somewhat smoother over time as well. This distinction is further illuminated in Fig. 4. Note how the error curves of all our estimation methods are fairly flat indicating a flow that approximates that of the actual vectors. In contrast, the nearest Euclidean distance mapping shows two humps that indicate frames where the actual trajectory has moved away from the estimate. The recursive filtered trajectories present the most consistent profile of all methods as well as the lowest overall error. Table I provides quantitative comparisons of the trajectory estimates for all five estimation methods illustrated in Figs. 2 and 3.

C. Sample Studies

The experiments of this section are intended to provide in-depth examinations of specific cardiac image sequences. The image sequences examined are gated MR short-axis acquisitions (256 × 256 pixels) of normal canine hearts. In general, image sequences are 16 frames long.

1) Qualitative: Qualitative assessments on trajectory estimates are made by examining the trajectory set as a whole for characteristics such as smoothness and plausibility. In general, vectors should not cross or drift together over time. General adherence to prominent shape features with a smooth flow among neighbors are the ideal characteristics.

Fig. 5 illustrates the estimated trajectories of various system configurations for a typical short-axis canine MR image sequence. The sequence begins showing the most expanded view of the LV, end-diastole (ED), cycling through the most contracted frame, end-systole (ES), and returns to ED. The results of the frame-to-frame methods on this study are presented in the upper two rows of Fig. 5. The Euclidean space method is particularly erratic in this contour sequence, indicated by the lack of trajectories in certain areas along the LV wall. Many of the trajectories finish the cycle far from their original starting position. The contour space method fares much better, providing stable trajectories all around the LV wall. There are still frequent instances of trajectories not returning to their origin, however, in general this condition does not appear to be as significant as with the Euclidean space method.

Trajectory estimates from various RLS filtering configurations are presented in the lower half of Fig. 5. One immediately notices how the RLS filter produces much smoother and realistic trajectories. There does not appear to be very much difference between the estimates employing the temporal model and spatiotemporal model in this study.

2) Marker Comparison: As discussed above, comparison with implanted markers provides a means for validating estimated trajectories, even though the extent of its usefulness is somewhat limited due to the lack of representation for other regions of the LV wall. This section will concentrate on examining specific cases of implanted trajectories and the error associated with estimated trajectories.

A graphic comparison between the trajectory of a single implanted marker and trajectory estimates from all the tracking methods is presented in Fig. 6. The most immediate observation is how well all the methods estimate the LV wall motion over the first nine frames. Although the Euclidean space method starts to drift off, it still maintains the relative flow of the marker trajectory. Unfortunately, the contour space method falls off the marker trajectory significantly after the ninth frame.

The performance of both RLS filtered approaches is outstanding. The spatiotemporal model estimate in particular almost exactly mimics the motion of the marker. Note that the gray levels of this marker—as with all markers in this article—were smoothed over before edges and boundaries were detected eliminating any possible bias the marker's shape might have provided. Thus, the trajectory of the marker had absolutely nothing to do with the estimate of this trajectory.

Error analysis of this marker comparison for each of the tracking methods is provided in Table II. As anticipated from Fig. 6, the spatiotemporal model offers the best performance in terms of mean error and error standard deviation.

Fig. 7 depicts a two-marker sequence in a comparison with each methods' estimates with their associated markers. In the case of the Euclidean space frame-to-frame approach, we observe that the trajectories diverge from the actual tracks soon into the sequence and complete the cycle far from their initial starting position. With the contour space approach, we note that the trajectories diverge as well though not as significantly.

Examination of the RLS filtered trajectory estimates versus the marker trajectories in Fig. 7 leads to some interesting observations. Although the spatiotemporal model drifts slightly from both marker trajectories over the cycle, the flow of the trajectory estimates is almost identical, even at sharp turns. The estimates for the temporal model are quite good as well, although the flow of the trajectories does not match that produced by the spatiotemporal model. Table III reconfirms the accuracy of the

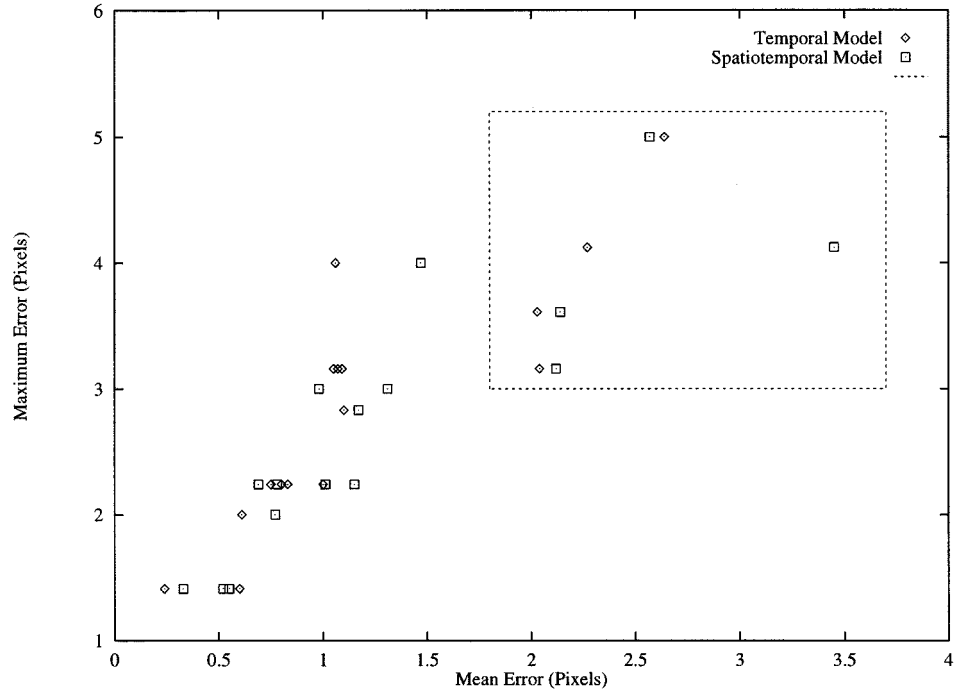

(a)

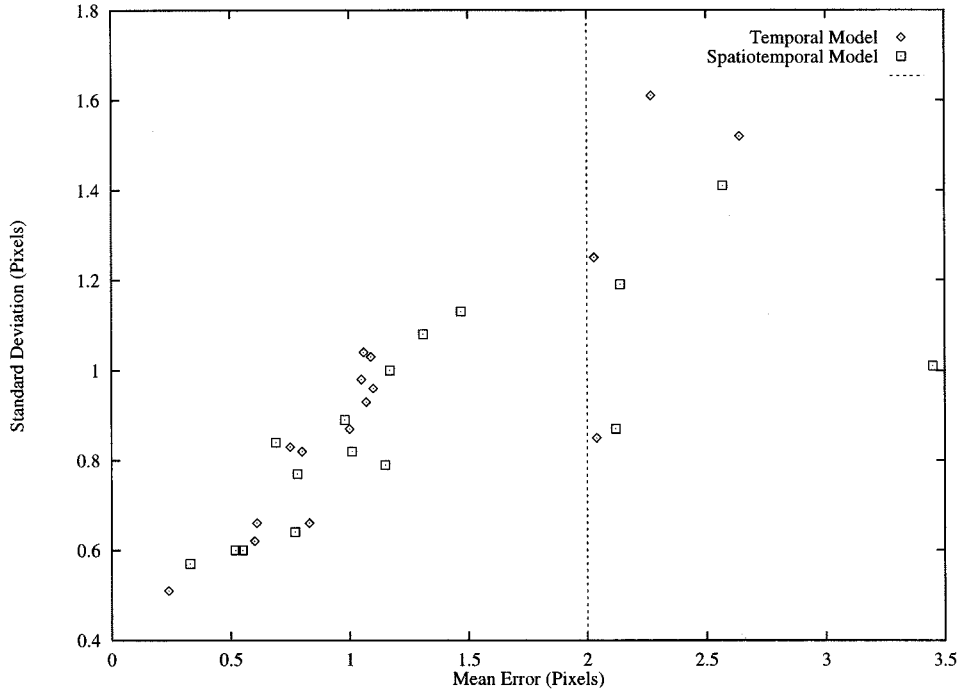

(b)

Fig. 8. (a) Plot of all cases of mean versus maximum error for the RLS filtered approaches. The data points enclosed in the box, indicate trajectory estimates of large error due to torsional motion missed by the local shape landmarks. (b) Plot of all cases of mean error versus standard deviation for the RLS filtered approaches. The data points to the right of the dotted line, indicate trajectory estimates of large error due to torsional motion missed by the local shape landmarks.

RLS filtered estimates discussed in Fig. 7 especially in terms of the flow criteria given by the standard deviation.

D. Ensemble Studies

The purpose of this section is to present a basic statistical analysis of tracking performance based on marker comparison for an ensemble of image sequences. Trajectory estimates from all four tracking approaches were collected and compared with 15 marker trajectories in 12 image sequences from seven normal canine hearts. MRI parameter settings remained consistent throughout all studies.

Fig. 8(a) depicts cluster plots of the mean error over a sequence versus the maximum single frame error within the same

TABLE IV
MARKER COMPARISON SUMMARY. COMPARISON OF PERFORMANCE ON DIFFERENT TRAJECTORY ESTIMATION METHODS. ALL VALUES ARE IN PIXELS. THE PHRASE "# BEST" IS USED TO INDICATE THE NUMBER OUT OF THE 15 TOTAL MARKER TRAJECTORIES IN WHICH A SPECIFIC METHOD OUTPERFORMED ALL OTHER METHODS FOR THAT ERROR MEASURE. *(E—EUCLIDEAN, S—CONTOUR, T—TEMPORAL MODEL, ST—SPATIOTEMPORAL MODEL)*

Method	# Best Mean Err.	Avg. Mean Error	Std. Dev. (Mean Err.)	# Best Std. Dev.	Mean Std. Dev.	Std. Dev. (Std. Dev.)
E	0	1.87	0.81	0	1.06	0.37
S	0	1.37	0.84	0	0.92	0.30
T	**8**	**1.18**	**0.72**	4	0.85	0.35
ST	7	1.28	0.90	**11**	**0.76**	**0.27**

sequence. Fig. 8(b) illustrates clusters of the mean error versus the standard deviation of error over a sequence. In general, both figures present a nice cluster of data in the lower left quadrant, indicating positive and consistent performance. Four of the 15 markers, however, yield very poor estimates. These cases highlight situations where a torsional component of motion exists that was not reflected in the movement of a characteristic shape feature along the wall. This is most likely an example of out-of-plane motion and further justification for extending the temporal models of this article to analysis of 3-D surface movement.

Examination of the graphics of Fig. 8 alone provides no discernible difference in positive performance between estimates of the temporal model and those of the spatiotemporal model. When examining negative performance data points (those further from the origin), however, the temporal model actually appears to hold an edge over the spatiotemporal model. Thus, when the spatiotemporal model performs poorly, it performs very poorly.

1) Performance Summary: Table IV provides a summary of the ensemble statistics analyzed in this section. Interestingly, RLS filtering using the temporal model provides the lowest average ensemble mean error. This can be reinterpreted to mean estimates using the temporal model land closer to the marker trajectories than any other approach.

Estimates from the spatiotemporal model clearly outperform the other approaches in terms of standard deviation of error. As stated above, standard deviation of error is a good indicator of flow, hence RLS filtering with the spatiotemporal model produces estimates that more closely approximate the flow of the marker trajectories.

V. SUMMARY

A flexible system for tracking pointwise nonrigid motion in image sequences has been presented, analyzed and shown to be useful in the application of tracking LV wall motion. This system takes as input a set of initial correspondences and accompanying descriptions of correspondence quality. It processes them with an adaptive filtering scheme using models for spatial and temporal smoothness and periodicity as appropriate, then produces a set of sinusoidal parameters that are transformed into quantified motion trajectories. The resultant trajectories are spatially and temporally smooth and periodically constrained. The system is not restricted to any one imaging modality and can be applied to any object undergoing nonrigid motion.

This system has been validated using MR image sequences containing MR contrast markers actually implanted in the LV wall. In most cases, this validation process has shown the system to be quite accurate. For this reason, the use of segment shape appears suitable for determining contour correspondence in this application. With four of the 15 compared markers, however, input comprised solely of shape-based correspondences produced estimates which completely missed the actual motion. These four marker trajectories exhibited a strong component of torsional motion (most likely due to 3-D out-of-plane motion). Consequently, a limitation of shape matching in 2-D is its inability to accurately capture torsional motion occasionally present in 3-D heart motion. However, 2-D motion captured in this way might be useful as a metric to compare visual motion in image sequences for database searching/sorting.

The heart is a 3-D object undergoing motion in three-dimensions. Our primary objective in this effort was to develop geometric techniques which could be extended to 3-D. The results of this work show considerable promise toward that end and present a strong argument for using an adaptive filter with a periodic temporal model when estimating the trajectories of heart wall motion in 2-D or 3-D.

This system establishes a framework from which a system for 3-D tracking might be constructed. Such a system is analyzed in more detail in [33]. In this circumstance, we're concerned with the correspondence of surface shape patches between surfaces at different temporal instances. The objective function combines a set of best-matched, shape-based motion correspondences with a weighting constraint based on the distance from immediate, neighboring surface patches. This objective function can be represented as a vector relationship which can be applied in similar fashion to the temporal model of this paper. Work in this area is ongoing.

In general, use of the temporal model is a prudent choice when implementing the RLS filter. Although use of a spatiotemporal model may offer some increased performance in instances of high quality contours with prominent shape variations, the performance gain does not seem so significant as to justify the additional computational cost.

In the future, new sources of correspondence could be used to improve incorporation of *a priori* knowledge, such as a method combining MR spin tags, shape and phase velocity information. Additionally, new applications of the system to analysis of other image-derived nonrigid object motion associated with the lungs and brain or microbic organizms present intriguing possibilities.

ACKNOWLEDGMENT

Dr. L. Staib's methods were used in segmenting the majority of contours used in experiments. Dr. A. Sinusas performed the surgery and supervised the imaging of the canine subjects used in our experiments. Dr. T. Constable conducted the imaging and provided assistance in processing and handling the data. The authors thank and appreciate each of these individuals for their assistance and insightful discussions.

REFERENCES

[1] J. S. Duncan, R. L. Owen, L. H. Staib, and P. Anandan, "Measurement of nonrigid motion using contour shape descriptors," in *Proc. IEEE Computer Vision Pattern Recognition*, Maui, HI, June 1991, pp. 318–324.

[2] J. C. McEachen, A. Nehorai, and J. S. Duncan, "Estimating cardiac motion from image sequences using recursive comb filtering," in *IEEE Int. Conf. Image Processing*, vol. 2, Washington, DC, Oct. 1995, pp. 496–499.

[3] J. C. McEachen and J. S. Duncan, "Shape-based tracking of left ventricular wall motion," *IEEE Trans. Med. Imag.*, vol. 16, pp. 270–283, June 1997.

[4] *IEEE Nonrigid and Articulated Motion Workshop*, J. K. Aggarwal and N. I. Badler, Eds. San Juan, PR, 1997.

[5] J. K. Aggarwal and N. I. Badler, "Articulated and elastic nonrigid motion: A review," in *IEEE Workshop Mot. Nonrigid Art. Obj.*, Austin, TX, Nov. 1994, pp. 2–14.

[6] D. Metaxas and D. Terzopoulos, "Shape and nonrigid motion estimation through physics-based synthesis," *IEEE Trans. Pattern Anal. Machine Intell.*, vol. 15, pp. 580–591, June 1993.

[7] T. McInerney and D. Terzopoulos, "A dynamic finite element surface model for segmentation and tracking in multidimensional medical images with application to cardiac 4d image analysis," *Comput. Med. Imag. Graph.*, vol. 19, pp. 69–83, Jan. 1995.

[8] D. Terzopoulos and R. Szeliski, "Tracking with kalman snakes," in *Active Vision*, A. Blake and A. Yuille, Eds. Cambridge, MA: MIT Press, 1992, pp. 3–20.

[9] S. Benayoun, C. Nastar, and N. Ayache, "Dense nonrigid motion estimation in sequences of 3d images using differential constraints," in *Lecture Notes in Computer Science: Computer Vision, Virtual Reality and Robotics in Medicine*. Berlin, Germany: Springer-Verlag, Apr. 1995, pp. 309–318.

[10] F. Leymarie and M. D. Levine, "Tracking deformable objects in the plane using an active contour model," *IEEE Trans. Pattern Anal. Machine Intell.*, vol. 15, pp. 617–634, June 1993.

[11] E. Bardinet, L. Cohen, and N. Ayache, "Superquadrics and free-form deformations: A global model to fit and track 3d medical data," in *Lecture Notes in Computer Science: Computer Vision, Virtual Reality and Robotics in Medicine*. Berlin, Germany: Springer-Verlag, Apr. 1995, pp. 319–326.

[12] M. Demi, R. Calamai, G. Coppini, and G. Valli, "A visual framework for the study of cardiac motion," *Comput. Cardiol.*, 1990.

[13] I. Cohen, N. Ayache, and P. Sulger, *Tracking Points on Deformable Objects Using Curvature Information*. Berlin, Germany: Springer-Verlag, 1992.

[14] P. Shi, G. Robinson, A. Chakraborty, L. Staib, R. Constable, A. Sinusas, and J. Duncan, "A unified framework to assess myocardial function from 4D images," in *CVRMed '95*. Nice, France, Apr. 1995, pp. 327–337.

[15] R. B. Schudy, "Harmonic surfaces and parametric image operators," Ph.D. dissertation, Univ. Rochester, Rochester, NY, 1981.

[16] W. Chen, G. B. Giannakis, and N. Nandhakumar, "Spatio-temporal approach for time-varying image motion estimation," in *IEEE Int. Conf. Image Processing*, vol. 2, Nov. 1994, pp. 232–236.

[17] A. Nehorai and B. Porat, "Adaptive comb filtering for harmonic signal enhancement," *IEEE Trans. Acoust., Speech, Signal Process.*, vol. 34, pp. 1124–1138, Oct. 1986.

[18] S. M. Seitz and C. R. Dyer, "Detecting irregularities in cyclic motion," *IEEE Works. Mot. Nonrigid Art. Obj.*, pp. 178–185, Nov. 1994.

[19] D. Gibson, T. Prewitt, and D. Brown, "Analysis of left ventricular wall movement during isovolumic relaxation and its relation to coronary artery disease," *Brit. Heart J.*, vol. 38, p. 1010, 1976.

[20] L. Axel and L. Dougherty, "MR imaging of motion with spatial modulation of magnetization," *Radiol.*, vol. 171, pp. 841–845, 1989.

[21] E. Zerhouni, "Tagging of the human heart by multiplanar selective RF saturation for the analysis of myocardial contraction," *Abstr. Annu. Meeting Soc. MR Imaging*, p. 10, 1988.

[22] J. Park, D. Metaxas, A. Young, and L. Axel, "Deformable models with parameter functions for cardiac motion analysis from tagged MRI data," *IEEE Trans. Med. Imag.*, vol. 15, pp. 278–289, June 1996.

[23] N. J. Pelc, A. Shimakawa, and G. H. Glover, "Phase contrast cine MRI," in *Proc. 8th Annu. SMRM*, Amsterdam, The Netherlands, 1989, p. 101.

[24] P. Van Dijk, "Direct cardiac nmr imaging of heart wall and blood flow velocity," *J. Comput. Assist. Tomogr.*, vol. 8, pp. 429–436, 1984.

[25] G. L. Nayler, D. N. Firmin, and D. B. Longmore, "Blood flow imaging by cine magnetic resonance," *J. Comput. Assist. Tomogr.*, vol. 10, pp. 715–722, 1986.

[26] N. J. Pelc, "Mycardial motion analysis with phase contrast cine mri," *SMRM, 10th Annu. Meeting*, p. 17, Aug. 1991.

[27] R. T. Constable, K. M. Rath, A. J. Sinusas, and J. C. Gore, "Development and evaluation of tracking algorithms for cardiac wall motion analysis using phase velocity mr imaging," *Magn. Reson. Med.*, vol. 32, pp. 33–42, 1994.

[28] J. McEachen, F. Meyer, R. Constable, A. Nehorai, and J. Duncan, "A recursive filter for phase velocity assisted shape-based tracking of cardiac nonrigid motion," in *5th Int. Conf. Computer Vision*, E. Grimson, Ed., Boston, MA, June 1995, pp. 653–658.

[29] P. Shi, "Image analysis of 3D cardiac motion using physical and geometrical models," Ph.D. dissertation, Yale Univ., New Haven, CT, May 1996.

[30] L. D. Cohen and I. Cohen, "A finite element method applied to new active contour models and 3D reconstruction from cross sections," in *Proc. 2nd Int. Conf. Computer Vision*, Tokyo, Japan, 1990, pp. 587–591.

[31] T. McInerney and D. Terzopolous, "A finite element model for 3d shape reconstruction and nonrigid motion tracking," in *Proc. 4th Int. Conf. Computer Vision*, Berlin, Germany, 1993, pp. 518–523.

[32] W. C. Huang and D. Goldgof, "Adaptive-size meshes for rigid and nonrigid shape analysis and synthesis," *IEEE Trans. Pattern Anal. Machine Intell.*, vol. 15, pp. 611–616, June 1993.

[33] J. C. McEachen, "Multiframe estimation of nonrigid motion from image sequences," Ph.D. dissertation, Yale Univ., New Haven, CT, May 1996.

[34] P. Clarysse, D. Friboulet, and I. E. Magnin, "Tracking geometrical descriptors on 3-D deformable surfaces: Application to the left-ventricular surface of the heart," *IEEE Trans. Med. Imag.*, vol. 16, pp. 392–404, Aug. 1997.

[35] G. J. Klein and R. H. Huesman, "A 3-D optical flow approach to addition of deformable pet volumes," *IEEE Work. Mot. Nonrigid Art. Obj.*, pp. 136–143, June 1997.

[36] L. H. Staib and J. S. Duncan, "Boundary finding with parametrically deformable models," *IEEE Trans. Pattern Anal. Machine Intell.*, vol. 14, pp. 1061–1074, Nov. 1992.

[37] J. S. Duncan, F. A. Lee, A. W. M. Smeulders, and B. L. Zaret, "A bending energy model for measurement of cardiac shape deformity," *IEEE Trans. Med. Imag.*, vol. 10, pp. 307–319, Sept. 1991.

[38] P. An, "A computational framework and an algorithm for the measurement of visual motion," *Int. J. Comput. Vis.*, vol. 2, pp. 283–310, 1989.

[39] N. Levinson, "The Wiener rms (root-mean-square) error criterion in filter design and prediction," *J. Math. Phys.*, vol. 25, pp. 261–278, 1947.

[40] S. S. Haykin, *Adaptive Filter Theory*. Englewood Cliffs, NJ: Prentice-Hall, 1986.

[41] T. Soderstrom and P. Stoica, *System Identification*. Englewood Cliffs, NJ: Prentice-Hall, 1989.

[42] E. C. Hildreth, *The Measurement of Visual Motion*. Cambridge, MA: MIT Press, 1984.

John C. McEachen, II (S'95–M'97) was born in Los Angeles, CA, on September 14, 1963. He received the B.S.E.E. degree from the University of Notre Dame, Notre Dame, IN, in 1985, the M.S.E.E. degree from the University of Virginia, Charlottesville, in 1990, and the M.Phil. and Ph.D. degrees from Yale University, New Haven, CT, in 1992 and 1995, respectively.

From 1985 to 1990, he served as a Cryptologic Officer in the U.S. Navy working with communications systems aboard submarines and surface ships. He was a National Library of Medicine Research Fellow from 1992 to 1995. In 1995, he was awarded a National Institutes of Health Post-Doctoral fellowship that he performed at Yale University. In 1996, he joined the civilian faculty of the Naval Postgraduate School, Monterey, CA, as an Assistant Professor of electrical and computer engineering. His teaching interests include image and video processing, computer networks, and communications systems. His research interests include video bitstream modeling and analysis in asynchronous transfer mode (ATM) environments, image sequence analysis using geometric models and adaptive estimation techniques, and ATM traffic modeling, monitoring and understanding.

Dr. McEachen is a member of Eta Kappa Nu and Tau Beta Pi.

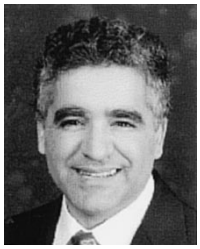

Arye Nehorai (S'80–M'83–SM'90–F'94) received the B.Sc. and M.Sc. degrees in electrical engineering from the Technion—Israel Institute of Technology, Haifa, in 1976 and 1979, respectively, and the Ph.D. degree in electrical engineering from Stanford University, Stanford, CA, in 1983.

After graduation, he was a Research Engineer for Systems Control Technology, Inc., Palo Alto, CA. From 1985 to 1995, he was with the Department of Electrical Engineering, Yale University, New Haven, CT, where he became an Associate Professor in 1989. In 1995, he joined the Department of Electrical Engineering and Computer Science, University of Illinois at Chicago (UIC), as a Full Professor. He holds a joint professorship with the Bioengineering Department at UIC. His research interests are in signal processing, communications, and biomedicine. He is an associate editor of *Circuits, Systems, and Signal Processing* and the *Journal of the Franklin Institute*. He is a member of the editorial board of *Signal Processing*.

Dr. Nehorai is the Editor in Chief of the IEEE TRANSACTIONS ON SIGNAL PROCESSING. He was an Associate Editor of the IEEE TRANSACTIONS ON ACOUSTICS, SPEECH, AND SIGNAL PROCESSING, IEEE SIGNAL PROCESSING LETTERS, the IEEE TRANSACTIONS ON ANTENNAS AND PROPAGATION, and the IEEE JOURNAL OF OCEANIC ENGINEERING. He served as Chairman of the Connecticut IEEE Signal Processing Chapter from 1986 to 1995 and is currently a Founding Member and the Vice-Chair of the IEEE Signal Processing Society's Technical Committee on Sensor Array and Multichannel (SAM) Processing. He is the co-General Chair of the First IEEE SAM Signal Processing Workshop which was held in March 2000. In 1979/1980 he received the Rothschild Fellowship in science and engineering, awarded annually to eight new graduates throughout Israel. He was co-recipient, with P. Stoica, of the 1989 IEEE Signal Processing Society's Senior Award for Best Paper. He has been a Fellow of the IEEE since 1994 and of the Royal Statistical Society since 1996.

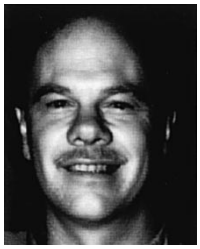

James S. Duncan (S'72–M'75–SM'93) was born in New York City on December 11, 1951. He received the B.S.E.E. degree from Lafayette College, Easton, PA, in 1973, the M.S. degree in engineering from the University of California, Los Angeles, in 1975, and the Ph.D. degree in electrical engineering from the University of Southern California, Los Angeles, in 1982.

In 1973, he joined the staff of the Electro-Optical and Data Systems Group, Hughes Aircraft Company, and participated in research and development projects related to signal and image processing for forward looking infrared (FLIR) imaging systems until 1983. During this time, he held Hughes' Masters, Engineer, and Doctoral Fellowships. In 1983, he joined the faculty of Yale University, New Haven, CT, where he is currently a Professor of diagnostic radiology and electrical engineering, and is the Director of the Image Processing and Analysis Group within Diagnostic Radiology. His research and teaching efforts have been in the areas of image processing, computer vision and medical imaging. His current specific research interests include the segmentation of deformable objects from both 2-D and 3-D data, the tracking of nonrigid object motion from 2-D and 3-D data, the use of physical models for recovering quantitative information from images and the integration of processing modules in vision systems, all with a special interest in using these approaches for medical image analysis. He is on the editorial board of the *Journal of Mathematical Imaging and Vision* and is co-editor of the journal *Medical Image Analysis.*

Dr. Duncan is a Member of Eta Kappa Nu and Sigma Xi and is an Associate Editor for the IEEE TRANSACTIONS ON MEDICAL IMAGING. He was inducted as a Fellow of the American Institute for Medical and Biological Engineering (AIMBE) in March 2000.